Comparison of pure and mixed gas permeation of the highly fluorinated polymer of intrinsic microporosity PIM-2 under dry and humid conditions: Experiment and modelling

Alessio Fuoco[a], Bekir Satilmis[b,c,**], Tamer Uyar[d], Marcello Monteleone[a], Elisa Esposito[a], Chiara Muzzi[a], Elena Tocci[a], Mariagiulia Longo[a], Maria Penelope De Santo[e], Marek Lanč[f], Karel Friess[f], Ondřej Vopička[f], Pavel Izák[f,g,h], Johannes C. Jansen[a,*]

[a] Institute on Membrane Technology (CNR-ITM), Via P. Bucci, 17/C, 87036, Rende, CS, Italy
[b] Institute of Materials Science & Nanotechnology, Bilkent University, Ankara, 06800, Turkey
[c] Department of Medical Services and Techniques, Vocational School of Health Services, Kirsehir Ahi Evran University, Kirsehir, 40100, Turkey
[d] Department of Fiber Science and Apparel Design, College of Human Ecology, Cornell University, Ithaca, NY, 14853, USA
[e] Department of Physics and CNR-Nanotec, University of Calabria, Rende, CS, Italy
[f] Department of Physical Chemistry, University of Chemistry and Technology Prague, Technická 5, Prague 6, 166 28, Czech Republic
[g] Institute of Chemical Process Fundamentals, Czech Academy of Sciences, Rozvojova 135, 165 02, Prague 6 – Suchdol, Czech Republic
[h] Institute of Environmental Technology VSB-TUO, 17. listopadu 15/2172, 708 33, Ostrava-Poruba, Czech Republic

ARTICLE INFO

ABSTRACT

This manuscript describes the gas separation performance of PIM-2, a partially fluorinated linear copolymer synthesized from 5,5′,6,6′-tetrahydroxy-3,3,3′,3′-tetramethylspirobisindane (TTSBI) and decafluorobiphenyl (DFBP). As one of the early members of the family of polymers of intrinsic microporosity, it had never been tested as a gas separation membrane because of insufficient mechanical resistance. This has been solved only recently, allowing the preparation of robust self-standing films. Molecular modelling studies demonstrated a high fractional free volume (34%) and an elevated surface area (642 $m^2\,g^{-1}$), and the latter is in good agreement with experimental BET results. Pure gas permeabilities measured on a fixed-volume time-lag instrument at 1 bar compare well with the results of mixed separation tests on a variable volume setup from 1-6 bar(a). Molecular modelling and independent sorption measurements on a gravimetric sorption balance both show strong dual-mode sorption behaviour, especially for CO_2 and to a lesser extent for CH_4. Temperature-dependent pure gas permeation measurements show typical Arrhenius behaviour, with a clear increase in the activation energy for diffusion with the increasing molecular size of the gas, indicating high size-selectivity. This is in agreement with the highly rigid PIM structure, determined by AFM force spectroscopy measurements. The dual-mode behaviour results in a moderate pressure dependence of the CO_2 permeability and the CO_2/N_2 and CO_2/CH_4 selectivity, all slightly decreasing with increasing pressure. The presence of humidity in the gas stream has a remarkable small effect on the membrane performance, which is probably due to the high fluorine content and the consequently low water vapour solubility in the polymer, as confirmed by gravimetric sorption measurements. The manuscript describes an extensive study on the structure-property relationships in PIM-2.

1. Introduction

Climate change and global warming are major concerns of our modern society, and anthropogenic greenhouse gas emissions are seen as one of their main causes. This urges for possible solutions to capture greenhouse gases or to reduce their emission. Membrane processes may offer an energy-efficient, environmentally benign and cost-effective solution [1–3], provided that membranes with a suitable combination of high permeability and high selectivity are used [4]. In 1991, Robeson recognized that there is a trade-off between permeability and

---

* Corresponding author. Institute on Membrane Technology (CNR-ITM), Via P. Bucci, 17/C, 87036, Rende, CS, Italy.
** Corresponding author. Department of Medical Services and Techniques, Vocational School of Health Services, Kirsehir Ahi Evran University, Kirsehir, 40100, Turkey

E-mail addresses: bekir.satilmis@ahievran.edu.tr (B. Satilmis), johannescarolus.jansen@cnr.it (J.C. Jansen).

selectivity, and he introduced a virtual upper bound for membrane performance [5]. Since then, there has been a continuous search for new membrane materials with increased performance, exceeding the upper bound. After their first introduction in 2004 by the group of Budd and McKeown [6,7], polymers of intrinsic microporosity (PIMs) have repeatedly broken the upper bound, leading to its continuous upward shift for different gas pairs [8,9], most recently for CO_2/N_2 and CO_2/CH_4 [10].

Because of their energy-efficiency, membranes for CO_2 separation are gaining importance in consolidated industrial processes such as CO_2 removal from natural gas [11,12], or in strongly emerging fields such as biogas up-grading [13]. A recent study to simultaneously purify CO_2 and CH_4 [14], not only exploits biomethane as a renewable fuel, but it also reutilizes CO_2 as a useful product. The most challenging and at the same time the most pressing application is CO_2 capture from pre- or post-combustion exhaust gas streams [15,16]. Besides dense polymeric membranes, different other concepts may be used, such as membrane contactors [17] or water-swollen reverse osmosis membranes [18], where the latter may be advantageous for the simultaneous removal of other undesired impurities, such as H_2S [19,20], thus reducing corrosion of pumps and pipelines, and increasing the lifetime of the membrane itself.

Many new membrane materials have been synthesized for CO_2/CH_4 and CO_2/N_2 separation [21]. Among these, PIMs are the strongest emerging group, thanks to their exceptionally high permeability and selectivity, in combination with their convenient solution-processability. Through the years, PIMs with many different chemical structures have been produced to improve continuously their gas transport properties (i.e. modification of the spiro-centre [22], introducing new monomers in the backbone [23–25] or spacers in side-chain [26], and finally by substitution of the nitrile groups with new functional groups [27–29]). Many of these studies benefit from extensive modelling approaches, which are the only method to visualize in detail the microstructure of the polymers [30,31], estimate the polymer-penetrant interactions [32], or calculate the permeability via molecular dynamics simulations [33]. Even if the predictive value is not very great, modelling provides valuable information on structure-property relationships.

Although it was part of the first generation of PIMs [6], the linear polymer synthesized from commercially available 5,5′,6,6′-tetrahydroxy-3,3,3′,3′-tetramethylspirobisindane (TTSBI) and decafluorobiphenyl (DFBP) monomers, and coded as PIM-2, was never tested for gas separation because of low molar mass and poor film-forming properties. Only recently, improved conditions of the synthesis led to the formation of a resistant, processable polymer [34], which has also been proposed for the formation of superhydrophobic electrospun fibrous membranes [35]. The hydrophobicity of PIM-2 prompted us to test the effect of water vapour on the gas separation performance of PIM-2 membranes in this work. Humidity in the feed gas is known to have a strong negative impact on the permeability in PIM-1 membranes [36]. In such cases, for a more efficient separation process, a pretreatment step is needed to remove most of the water from the feed stream. Therefore, the development of a membrane of which the permeability and selectivity are less sensitive to the presence of water could offer a great technological benefit.

The scope of this manuscript is the thorough screening of this previously ignored PIM-2 as a membrane material, with emphasis on two separations of major interest for a sustainable future: CO_2/CH_4 separation for biogas upgrading, and CO_2/N_2 separation for CO_2 capture from flue gas. A further aim is the investigation of its structure-property relationships via experimental and computational analysis of its structure, its rigidity and its pure and mixed gas permeability, comparing dry and humid CO_2/N_2 (15/85 vol%) and CO_2/CH_4 (35/65 vol%) mixtures that simulate the compositions of flue gas and biogas, respectively.

2. Experimental

2.1. Materials

The synthesis of PIM-2 (Fig. 1) was performed by the previously described method [34,35]. Briefly, TTSBI (2.04 g, 6 mmol) and K_2CO_3 (0.83 g, 6 mmol) were placed in a 250 mL three-necked round bottom flask equipped with a reflux condenser, and magnetic stirring-bar. Then, 12 mL of anhydrous DMF was added under argon atmosphere with the help of a plastic syringe and needle. The mixture was heated to 100 °C in an oil bath for 30 min to ensure complete dissolution. Simultaneously, DFBP (2.0g, 6mmol) was dissolved in 58 mL anhydrous DMF at room temperature and transferred into the reaction mixture drop-wisely using a syringe pump (12 mL plastic syringe and 20 mL h^{-1} flow rate). The reaction was maintained at 100 °C for 48 h until an off-white suspension was obtained. Then, it was poured into 150 mL of aqueous HCl (5%) and the precipitate was filtered by a sinter funnel under vacuum. The crude product was dried at 150 °C overnight in a standard laboratory oven and was then washed with methanol to remove any unreacted species from the polymer, and finally dried overnight at 110 ºC. The final product (94% yield, 3.35 g) was further purified by dissolving in $CHCl_3$ and reprecipitating in methanol.

Agilent gel permeation chromatography (GPC) equipped with a ZORBAX PSM 300-S column was used to determine the molecular weight of the PIM-2. THF was used as a mobile phase and the calibration was performed using polystyrene samples with different molecular weights. The chemical structure and functional groups of PIM-2 were investigated using a Bruker Vertex70 FTIR Spectrometer in transmittance mode. ^{1}HNMR and ^{19}FNMR spectra were recorded in $CDCl_3$ on a Bruker DPX-400 MHz NMR spectrometer. A Thermo Fisher Scientific K-alpha XPS Spectrometer equipped with monochromatic Al K-alpha source was employed for elemental analysis of the PIM-2 samples. N_2 sorption isotherms were determined on a Quantachrome Autosorb iQ gas sorption analyser. The analysis was performed at 77 K after degassing the samples for 16 h at 120ºC.

2.2. Membrane preparation and characterization

PIM-2 powder (∼0.2 g) was dissolved in 5 mL of $CHCl_3$ and stirred well for overnight. Then the solution was filtered through wool into a 6 cm glass petri dish and it was slowly evaporated for 48 h. The membranes were further dried in an oven at 110 °C for 4 h. Before the gas permeation measurements, all membrane samples were first soaked in anhydrous methanol for 24 h and then dried for 24 h at 25 °C and
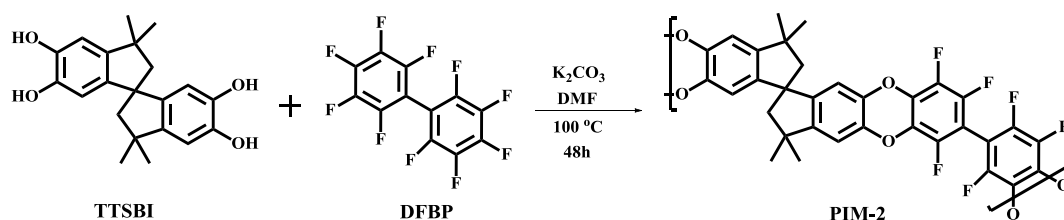

Fig. 1. Synthesis path and chemical structure of PIM-2.

ambient pressure. It was observed that the sample absorbed ca. 30 wt% of MeOH, causing a volumetric swelling of ca 50%, facilitating the removal of residual casting solvent, as in other PIMs [37]. For further stabilization, samples were dried at 30 °C under vacuum for 72 h.

2.2.1. Force spectroscopy

The elastic modulus was measured in air at room temperature on a Multimode 8 AFM system with a Nanoscope V controller, by the method reported elsewhere [38]. Cantilevers CP-PNP-SiO (SQUBE), with a spherical tip and a nominal radius of 1000 nm ($\pm 5\%$), were used. The cantilever, with an elastic constant of $62\,\mathrm{N\,m}^{-1}$, was calibrated using the appropriate calibration probes (CLFC, Force calibration cantilevers, Bruker) in accordance with producer's instructions [39]. The local elastic modulus, E, was calculated by fitting the single Force-Deformation curve (FD) with the Hertz model [40], which predicts that the force increases non-linearly with the indentation depth, δ:

$$F = \frac{4}{3} \frac{E\sqrt{r\delta^3}}{(1 - \upsilon^2)} \tag{1}$$

where F is the loading force, r is the tip's radius of curvature. The parameter υ is the Poisson's ratio, which compares the strains in the transverse and longitudinal directions under uniaxial stress and is assumed to be 0.3 in the case of glassy polymers [41]. For each membrane, 60 FD curves were recorded after the permeation tests, on three different areas and at a scan rate of about $400\,\mathrm{nm\,s}^{-1}$. Data were fitted using the NanoScope Analysis 1.5 software and the results were statistically analysed using Microsoft Excel.

2.3. Gas transport properties

2.3.1. Single gas permeation

Single gas permeation measurements were performed at three different temperatures (from 15 to 35 °C) and at 1 bar on a constant volume/pressure increase instrument by the time lag method (Elektro & Elektronik Service Reuter, Geesthacht, Germany). Measurements at different pressures were performed on a variable volume/constant pressure instrument, equipped with a quadrupole mass filter (HPR-20 QIC Benchtop residual gas analysis system, Hiden Analytical), in a cross-flow cell with argon as the sweeping gas. The methods are described in detail by Fraga et al. [42]. All gases were supplied by Sapio (Italy) at a minimum purity of 99.9995 + %.

2.3.2. Mixed gas permeation

Mixed gas permeation measurements were performed on a variable volume/constant pressure instrument in a cross-flow cell with argon as the sweeping gas and different feed pressures and/or feed compositions. The permeate is measured continuously by means of a mass-spectrometric residual gas analyser (HPR-20 QIC Benchtop residual gas analysis system, Hiden Analytical). Measurements were performed at high feed flow rates and relatively high sweep flow rates at a low stage cut, near 1% or lower, and a negligible partial pressure in the permeate, in order to avoid polarization phenomena. Details of the method, the instrument specifications and the calibration were described previously [42,43]. For this work, the setup was equipped with an additional gas humidifier (Figure SI1) consisting of two stainless steel bubble columns and a third vessel to avoid water droplets in the line. A bypass allows quick switching between dry and humid gas streams and a vent allows saturation of the feed gas before exposure of the membrane. The gases were supplied by Sapio (Italy) at a minimum purity of 99.9995 + %.

2.3.3. Gas sorption

Gravimetric sorption experiments of CO_2, CH_4, N_2 and H_2O at 25.0 ± 0.1 °C, were performed using a custom-made apparatus, equipped with a calibrated McBain quartz spiral balance. Details can be found elsewhere [44]. The PIM-2 sample was attached to the end of the

spiral in a glass measuring chamber, which was evacuated before each measurement to a pressure lower than 10^{-3} mbar by a rotary oil pump (Trivac D4B, Oerlikon Leybold). A Leybold oil mist filter was mounted on the pump to avoid contamination of the measuring chamber with oil vapours from the pump (with 99.99% efficiency). The sorption experiments were performed at the absolute pressure ranging from vacuum up to 12 bar. The corresponding elongation of the quartz spiral was recorded by a charge-coupled device (CCD, Sony), which allows the determination of gas sorption with a maximum experimental error of ca. 30 μg.

2.4. Molecular modelling

The simulations were performed with the Materials Studio 7.0 software package (Accelrys) [45]. The force field used was the Condensed-phase Optimized Molecular Potentials for Atomistic Simulation Studies (COMPASS) [46], a force field suitable to explore polymer properties in general [47,48] and also those of PIMs [24,32,49,50]. Materials studio's Amorphous Cell tool was used to set 3D periodic boundary conditions while filling the boxes with polymer [45]. The algorithm grows the chain molecules in the box, one segment at the time, with random torsion, by Monte Carlo moves. The probability of the Monte Carlo algorithm is calculated with respect to Flory's RIS theory [51]. Three polymer chains of 30 repeating units and 400 argon atoms were inserted in each box. Argon atoms act as solvent-like particles [52,53], in order to mimic the experimental reality of solvent casting and to suitably keep the chains mutually distant, preventing overall misplacement.

Three boxes were selected among the 50 created, by a preliminary test of their fractional accessible volume (FAV) [53], defined as:

$$FAV = \frac{(V_T - V_{SA})}{V_T} \tag{2}$$

where V_{SA} is the solvent accessible volume and V_T is the total volume of the model box. The solvent accessible volume is defined by a scaled (with respect to probe radius) van der Waals volume. Some internal voids could be inaccessible to the probe and can be excluded from the measurement.

The three boxes were equilibrated via a series of temperature cycles at 50 bar, in a temperature range of 450 K–300 K. At each temperature cycle, some argon atoms were eliminated from the structure, simulating the evaporation process. Finally, NPT dynamics of 300 ps were performed to further equilibrate the boxes at 300 K and 1 bar. Box details are summarised in Table 1.

2.4.1. Fractional free volume and nitrogen surface accessible area

The fractional free volume (FFV) was evaluated via Materials Studio's "Atom Volumes & Surfaces" tool at 298 K [45]. The van der Waals volume (V_{VdW}) is measured for each box and the FFV is calculated via Eq. (3):

$$FFV = \frac{(V_s - 1.3V_{VdW})}{V_s} \tag{3}$$

where V_s is defined as reciprocal density [54]. The factor 1.3 is a universal packing factor that transforms the V_{VdW} in the occupied volume. This universal packing factor is usually referred to as Bondi packing factor [55]. The N_2 surface accessible area (for Brunauer-Emmett-Teller

Table 1
Computational details of the molecular models.

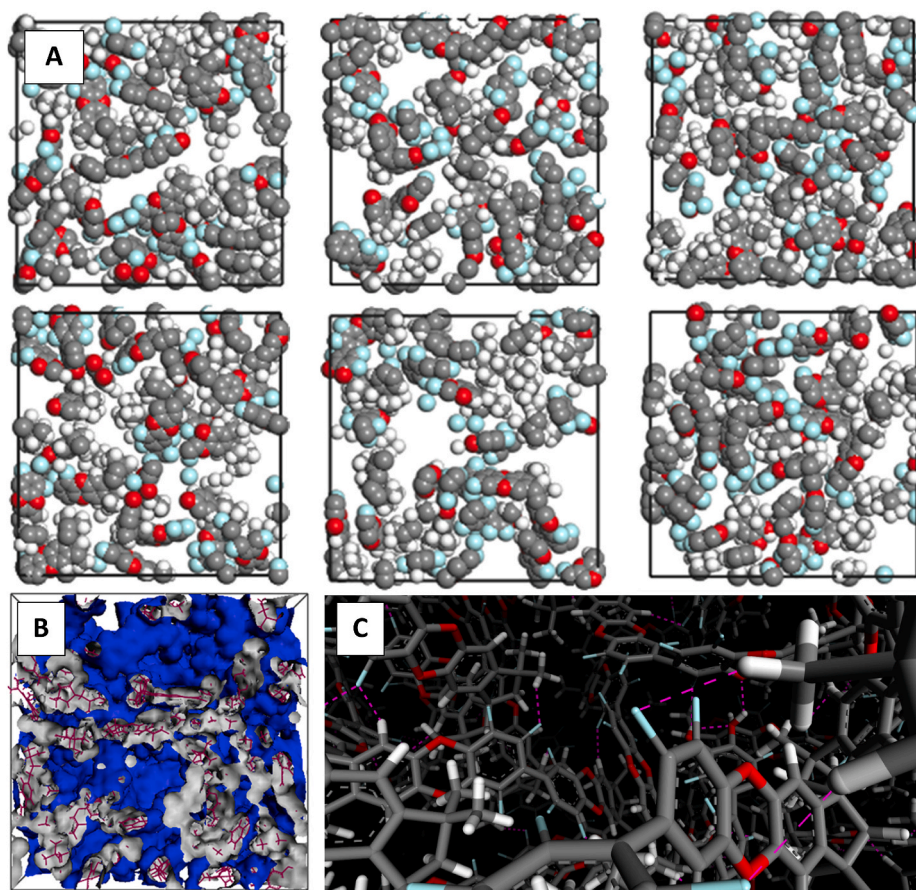|	
Average side length (Å)	43.3 ± 0.4
Number of atoms in each chain	1896
Number of chains	3
Total number of atoms	5688

Fig. 2. (A) Molecular model showing six successive slices of a polymer 'box', cleaved in the x-direction every 4.82 Å, corresponding to 1/9th of the total side length. Atoms are reported in CPK style with their van der Waals radii. (B) The van der Waals isosurface separating the volume "occupied" by chains and the complementary free volume, as perceived by a punctual probe. The isosurface is grey inside (facing polymer) and blue outside. (C) Detailed snapshot of molecular packing showing halogen and hydrogen bonds between hydrogen and fluorine atoms and between hydrogen and oxygen atoms, respectively. Hydrogen bonds in pink colour, fluorine atoms in cyan, oxygen atoms in red, carbon atoms in grey, hydrogen atoms in white. (Settings: maximum hydrogen-acceptor distance 2.5 Å, Minimum donor-hydrogen-acceptor angle 90.0°). (For interpretation of the references to colour in this figure legend, the reader is referred to the Web version of this article.)

-BET-area evaluation) was measured according to Teplyakov-Meares' radii [56]. The "(accessible) solvent surfaces" routine calculates the accessible area described by the probe centre as it rolls over a scaled (with respect to probe radius) van der Waals surface.

2.4.2. Sorption isotherms

Sorption isotherms were calculated via Materials Studio's Sorption module [45]. The solubility coefficients were calculated from the low-pressure limit of penetrant molecules concentration, C(p)/p, in the adsorbent framework. Configurational bias task [57] was used, with 10,000 equilibration steps and 300,000 production steps. Sorption runs were performed from 0.10 bar to 10 bar at 298 K.

2.4.3. Diffusion coefficients

Dynamics runs for the calculation of the diffusion coefficient were performed in the limit of low concentrations where gas particles do not mutually interact. For these experiments, a number of He, H_2, Ne, O_2, Ar, N_2, CH_4 and CO_2 gas molecules were inserted into the boxes. Based on preliminary tests of gas sorption in the limit of 0 bar, five molecules of helium and ten molecules of all other gases were used. Under these conditions, it was also possible to fill boxes with couples of gases and still study them independently. A total of 15 boxes was prepared, using three chosen boxes five times each. Gas particles were placed randomly in the boxes. A production dynamics was performed via Forcite module at 298.15 K, 1 bar and 10 ns. The dynamics of He, Ar and Ne were stopped at 5 ns because they were already in the diffusive regime

[58,59]. A group-based calculation method was used to calculate non-bonded interactions with a 22 Å cut-off and a 1 Å spline width. Nose thermostat and Berendsen barostat were set [60,61]. The diffusion coefficients (*D*) were calculated by Einstein's equation (Eq. (4)) [62] that links the mean square displacements (*MSD*) of the investigated particles with their number (*N*) in the system, via:

$$D = \frac{1}{6N} \lim_{t \to \infty} \frac{d}{dt} \langle \sum_{i=0}^{N} (r_i(t) - r_i(0))^2 \rangle \tag{4}$$

The term in angular brackets is the mean square displacement, calculated for each molecule for different initial conformations ($r_t = 0$) and averaged on the ensemble of molecules.

3. Results and discussion

3.1. Membrane preparation and conditioning

The PIM-2 powder and membrane samples were characterized by FTIR, XPS, ^{1}H NMR and ^{19}F NMR. The results are reported in the supporting information in Figure SI2 and Table SI1, which are consistent with previous study [35]. The increase of the reaction time from 24 h in the previous study to 48 h in this work resulted in a slight increase in the molar mass of the polymer from $M_n = 5800 \, \text{g mol}^{-1}$ and PDI = 4.7, to $M_n = 6100 \, \text{g mol}^{-1}$ and PDI = 4.9. Although these values are still lower than the molar mass of the first PIM-2 produced by Budd

Table 2
BET Surface area ($m^2 g^{-1}$) and FFV (%) of PIM-1 and PIM-2.

	Method	PIM-1	Polymer PIM-2
BET Surface area	Experimental	850 [6]	600 [6]
			615 [35]
			636 [This work]
	Computational*	n.a.	642 [This work]
	Computational**	595 [31]	410 [This work]
FFV		24.3% [31]	34.2 ± 5.3% [This work]
		28.8% [65]	

*Effective diameter d_{N2} = 3.040 Å [56], **Kinetic diameter d_{N2} = 3.681 Å [67].

et al. [6], the polymer was sufficiently flexible to produce robust self-standing films by solution casting from chloroform (Figure SI3). This suggests the formation of a more linear backbone with less branching, allowing the formation of more entanglements between the polymer chains, with respect to earlier work, where PIM-2 was reported as a non-film-forming polymer [6]. The differences in the present work are the longer reaction time and dropwise addition of fluoro-monomer into the spiro-monomer solution, similar to the procedure of Sato et al. [34]. This was previously suggested by Zhang et al. as a strategy to synthesise perfectly alternating PIMs [63]. AFM force spectroscopy analysis gave a Young's modulus of 2.16 ± 0.03 GPa for the methanol treated sample (Figure SI5). This is one of the highest values reported for PIMs [26,64], and it further increases upon thermal conditioning and upon ageing of the sample. The high Young's modulus and its bendability (Figure SI3) make PIM-2 suitable for membrane preparation.

3.2. Microstructure

Nitrogen adsorption/desorption measurements were performed on powder and membrane samples. The BET surface area of the PIM-2 powder was 636 $m^2 g^{-1}$ (Figure SI4), in good agreement with previous studies [6,35]. The BET surface area of the PIM-2 membrane could not be measured under the same conditions because of the extremely slow sorption kinetics at the temperature of liquid nitrogen in thick dense films. Fig. 2 A and B show the inefficient packaging of PIM-2, resulting in a large fractional free volume (FFV) with interconnected voids in the polymer network. The computed FFV of PIM-2 is about 34% (Table 2) which is larger than that of PIM-1 [31,65] or PIM-EA-TB [66], and similar to that computed for the ultrapermeable PIM-TMN-Trip [26]. The theoretical Brunauer-Emmett-Teller (BET) surface area of PIM-2 (642 m^2g^{-1}, Table 2 and Fig. 2B) is within the lower range of BET surface areas reported for PIMs, but is in excellent agreement with our experimental value of 636 $m^2 g^{-1}$. High FFV and relatively low BET surface area are an indication of the presence of large voids with limited interconnectivity, as shown in the slices of the molecular model (Fig. 2A). This unexpected low interconnectivity can be attributed to the additional presence of halogen-bonds in the polymer matrix due to the presence of fluorine atoms (Fig. 2C), that enhance the intra- and interchains interactions.

The theoretical BET surface area computed with Teplyakov and Meares' diameter [56] is in much better agreement with the experimental values than that calculated with the traditionally used Breck diameter [67], which underestimates the BET surface area (Table 2). This indicates that T-M diameters are more suitable for the correlation of the penetrant gas and PIM-2 properties. This was recently demonstrated to be generally true for PIMs [68], where they give a better correlation between the molecular size and the experimental diffusion coefficients. This is further confirmed by the good correspondence of the trend in the simulated and experimental diffusion coefficients as a function of the T-M diameter (Fig. 3A).

Single gas permeability measurements show that a freshly

methanol treated film of PIM-2 is most permeable to CO_2 (P_{CO_2} = 6600 Barrer), and the order of gas permeabilities is $CO_2 > H_2 > He > O_2 > CH_4 > N_2$ (P_{N_2} = 460 Barrer, Table SI2). Based on the very high FFV, one might have expected a higher permeability, but the combination with the relatively low BET surface area in PIM-2 leads to gas transport properties which fall in the classical region of spiro-based PIMs. He and O_2 permeability are inverted with respect to PIM-1, showing that size selectivity plays a crucial role in the gas transport in PIM-2.

This is further confirmed by the gas diffusivities in PIM-2, which decrease as a function of the effective diameters (Fig. 3A), following a similar non-linear trend as that observed for other PIMs [10,26,69], and with absolute values close to that of PIM-1 [26,70–72]. The diffusion coefficients derived from MD simulations follow the same trend and are in good quantitative agreement with the experimental data for smaller gas molecules (Fig. 3A), losing some precision on the bulker penetrants like CH_4. Besides increased resistance to transport of larger molecules, part of the loss in the diffusion coefficient is also due to the decrease of the fractional accessible volume for bulkier gases (Fig. 3B).

Both experimental and computed equilibrium sorption isotherms exhibit typical dual-mode behaviour for all gases, with exception of the computed H_2 sorption that follows Henry's law (Fig. 4A and B). Gravimetric sorption of CO_2, methane and nitrogen shows very quick kinetics, which does not allow accurate calculation of the diffusion coefficients. Water sorption shows unusual behaviour: the kinetics of water sorption is extremely fast, and approximately 0.25 mg g^{-1} of water is absorbed within seconds, before damping of the spring. The very quick absorption of a small amount of water is in line with the small dimensions of the water molecule (d_{eff} = 2.61 Å [56]), for which a diffusion coefficient similar to that of hydrogen and helium is expected. Indeed, close examination of the early stage of the time lag curve for water vapour permeation shows a very short transient (Figure SI6A). Although the time lag of water is not as short as that of He and H_2 but of the same order of magnitude as that of oxygen (Figure SI7), it still confirms rapid diffusion. However, sorption continues with much slower kinetics for several hours. Also for water vapour permeation, after the rapid initial permeation, the slope of the time lag curve continues to increase slowly for over 20 min, leading to an apparently much longer time lag and lower diffusion coefficient (Figure SI6B). This is a similar phenomenon as that described previously for diffusion of C_1–C_6 alcohol vapours in the highly hydrophobic glassy perfluoropolymers Hyflon®AD80x [73], and Teflon AF 2400 [74], where single molecules have a high diffusion coefficient, but cluster formation significantly reduces the effective diffusivity and leads to an apparent spectrum of diffusion coefficients [73,74]. Even slower phenomena may be related to relaxation processes of the polymer itself, leading to slow dilation of the polymer matrix or to reorientation of the polymer segments, and resulting in a further increase in H_2O vapour solubility as a function of time.

The theoretical and experimental solubility coefficients are in good agreement with each other (Fig. 4C), and the slight scattering between the data can be attributed to small differences in the sample history and different methods of evaluation. For all methods, the order of the solubility coefficients is $CO_2 > CH_4 > O_2 > N_2 > H_2$, and their trend as a function of the gas critical temperature is typical for polymer membranes that do not specifically interact with the gas penetrant [75]. In absolute values, the CO_2 solubility in PIM-2 is higher than that in traditional polymers used for gas separation [76], but it is low when compared to other PIMs, especially in consideration of its very high FFV. The stabilization treatment hardly influences the gas solubilities, which almost overlap with those of the freshly treated sample (Fig. 4C), in contrast with the strong change in diffusion coefficients (Fig. 3A). The low gas uptake is due to partially fluorinated nature of PIM-2 (Fig. 1). Electronegative fluorine atoms are more likely to undergo intramolecular interactions (Fig. 2C) than interactions with surroundings particles. Thus, the affinity between the polymer and penetrant gas is
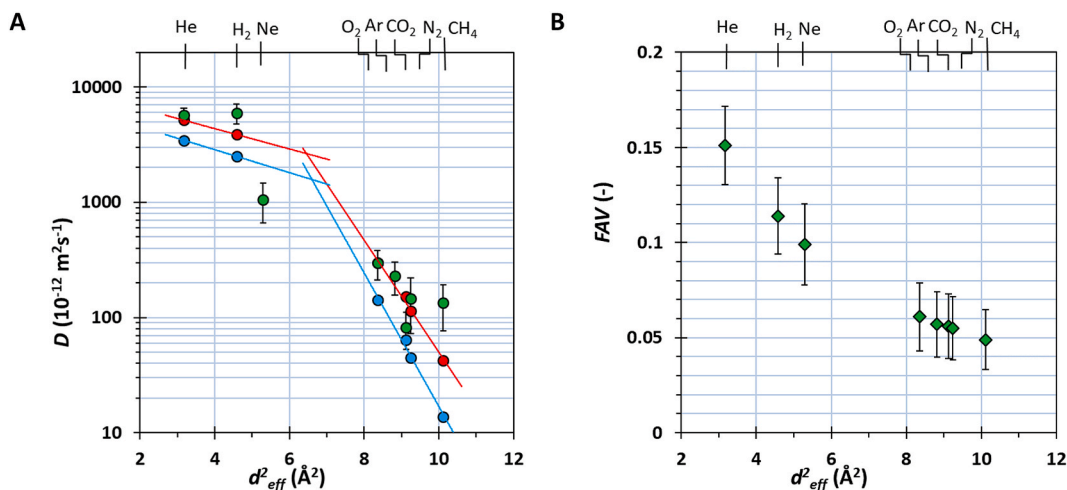
Fig. 3. (A) Simulated diffusion coefficients (●) and experimental values determined by the time lag method for the freshly treated sample (●) and the stabilised sample (●) at 1 bar. (B) Simulated fractional accessible volume (FAV) for probes of different dimensions (◆).
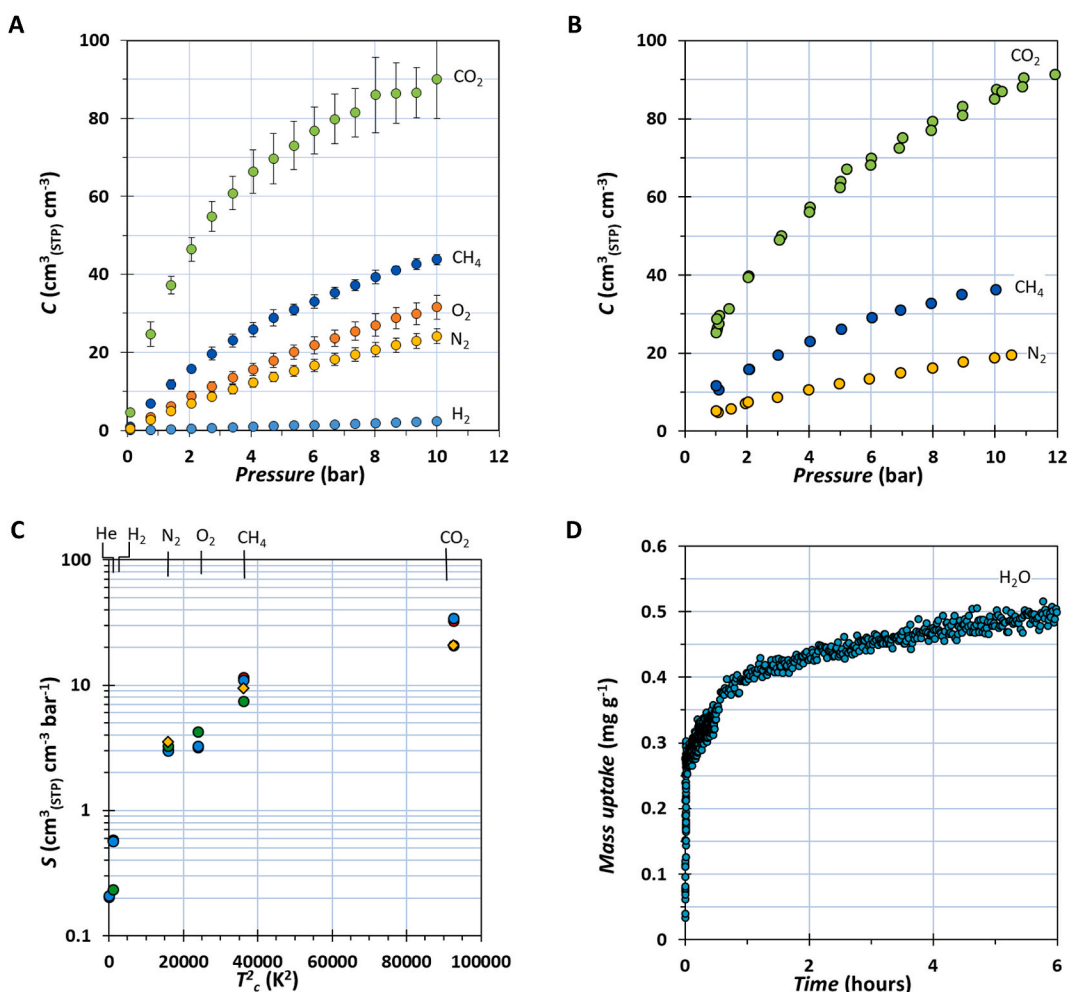

Fig. 4. (A) Simulated sorption isotherms of CO_2, CH_4, O_2, N_2 and H_2; (B) experimental sorption isotherms for CO_2, CH_4 and N_2; (C) calculated solubility (●), experimental solubility at 1 bar from gravimetric sorption measurements (◆) and from the time lag experiments the freshly treated sample (●) and the stabilised sample (●) as a function of the squared critical temperature and (D) sorption kinetics experiment for water vapour.

hindered. Although the highly polarizable CO_2 interacts with the polar dioxane groups of the polymer chain, as indicated by their position in the optimized molecular models (Figure SI8). Dioxane-CO_2 interaction was found to be weak with respect to the interaction between CO_2 and N-containing groups [32] usually present in PIMs structures.

The stabilised membrane was tested in the temperature range of 15 °C–35 °C, and data are plotted in Fig. 5. This range offers a good compromise between permeability, selectivity and energy costs. For instance biogas production usually takes place at temperatures around 35 °C, with a maximum up to 50 °C [77]. Although energy is required to
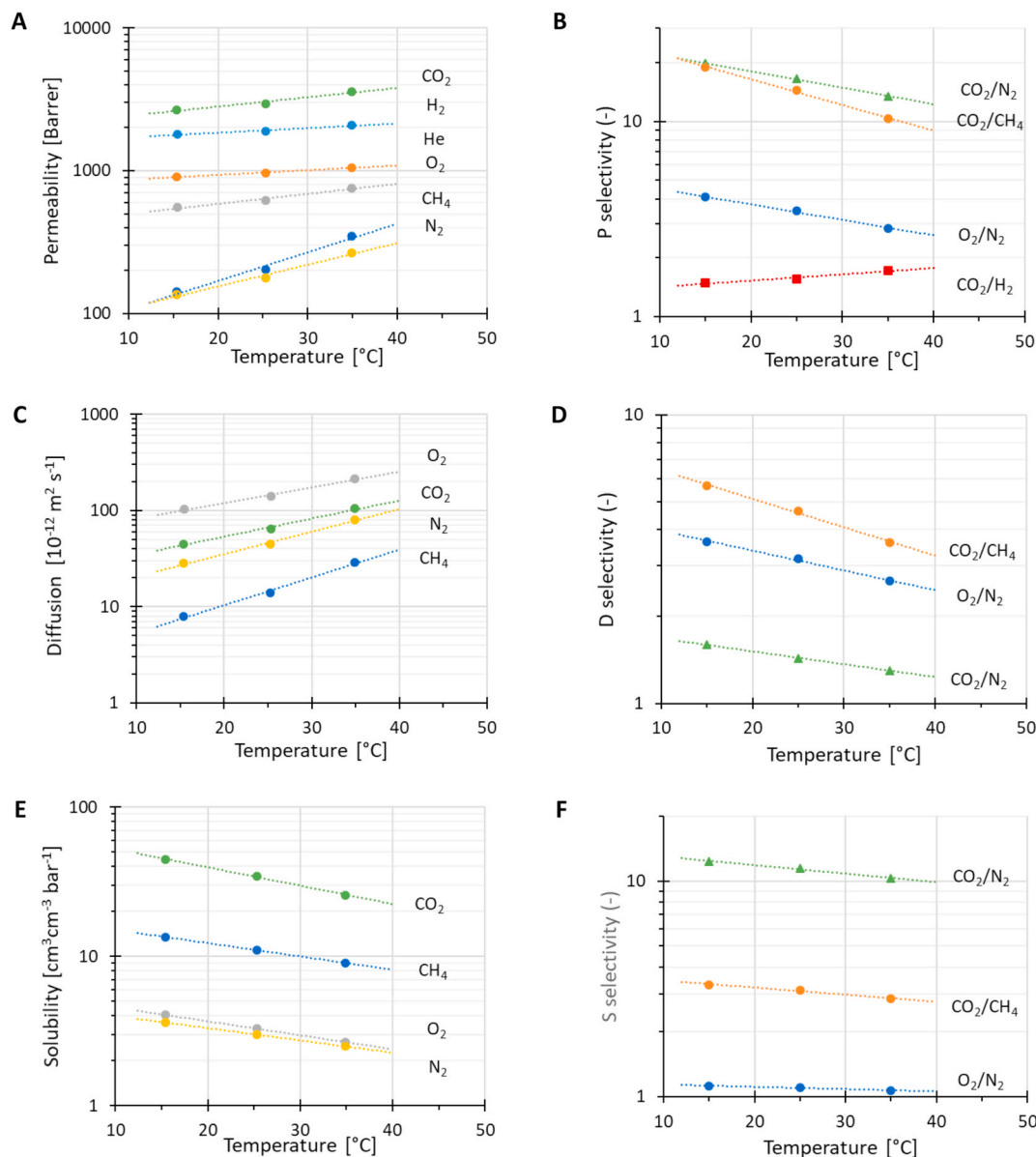
Fig. 5. Temperature dependence of (A) permeability, (C) diffusion, (E) solubility and their corresponding selectivities (B), (D) and (F) in the PIM-2 membrane dried at 30 °C for 72 h under vacuum after methanol treatment. Numerical data are given in Table SI2 and the corresponding Arrhenius plots in Figure SI9. Lines are plotted as a guide to the eye.

Table 3

Activation Energies for Permeation (E_p) and Diffusion (E_d), Heat of Sorption (H_s), Diffusion Selectivity (D_i/D_{N2}) and Correlated *Energetic* and *Entropic Selectivity* with respect to N_2 at 25 °C in PIM-2 after stabilization.

Gas	E_p	H_s	E_d	D_i/D_{N2}	*Entropic Selectivity*	*Energetic selectivity*
	(kcal mol^{-1})	(kcal mol^{-1})	(kcal mol^{-1})	(−)	(−)	(−)
N_2	6.14	−3.34	9.48	–	–	–
O_2	2.85	−3.79	6.64	3.17	0.029	121
CO_2	2.64	−4.99	7.62	1.43	0.063	23
CH_4	8.11	−3.62	11.7	0.31	12.5	0.023

cool the gas mixture, the selectivity for CO_2 is higher at low temperature, and cooling has the additional advantage that it removes most water vapour and low-volatile organic compounds by condensation [14]. Similarly, flue gas is produced at higher temperatures, but the membrane selectivity is much higher at lower temperature as in this case (Fig. 5B), both by increased diffusion selectivity (Fig. 5D) and

increased solubility selectivity (Fig. 5F). The permeability and the diffusivity increase with temperature (Fig. 5A and C) while solubility decreases (Fig. 5E). The calculated activation energies for permeation and diffusion, and the heat of sorption were calculated on the basis of the observed temperature dependence (Table 3), and this offers the possibility of a reasonably reliable prediction of the permeability by

extrapolation to higher or lower temperature.

The activation energy of permeability (E_P, Table 3) is positive for all gases and among the highest values known for PIMs, while heats of sorption are in the typical range for PIMs [78,87]. The high E_p in PIM-2, Eq. (5), is mostly due to its high activation energy of diffusion, which is higher than in PIM-1, and it shows also a steeper slope with increasing gas dimensions (Figure SI10).

$$E_P = E_d + H_s \qquad (5)$$

This evidences that the PIM-2 is even more size-selective than PIM-1. The diffusion selectivity can be expressed in terms of entropic and energetic selectivity [80] (Eq. (6)):

$$\frac{D_x}{D_y} = \underbrace{\frac{\lambda_x^2}{\lambda_y^2}\exp\left(\frac{\Delta S^*_{d(x,y)}}{R}\right)}_{entropic\ selectivity}\underbrace{\exp\left(-\frac{\Delta E^*_{d(x,y)}}{RT}\right)}_{energetic\ selectivity} \qquad (6)$$

where λ is the average diffusive jump length, R the universal gas constant, T the absolute temperature, $\Delta S^*_{d(x,y)}$ the difference in the activation entropy of diffusion for two gases (x and y), and $\Delta E^*_{d(x,y)}$ is the difference in E_d between the two gases. Thus, the size-selectivity in PIM-2 arises from the energetic contribution of the diffusion coefficient (Table 3), which value is higher than in PIM-1, meaning that more energy is required for the opening of the motion enabled zones in PIM-2 with respect to PIM-1 [78]. Remarkably, the O_2/N_2 energetic selectivity in the spiro-based PIM-2 is higher even with respect to that of the very rigid benzotriptycene-based PIMs [78], implying that the energetic contribution must not be ascribed only to the polymer chain rigidity,

but also to intra and interchain interactions. Molecular modelling highlights the presence of a diffuse network of hydrogen and halogen bonds hindering the probability to create motion-enable zones by the higher cohesion energy between polymer chains, and increasing the energetic selectivity.

3.2.1. Mixed gas permeation

For the mixed gas permeation measurements, in a single experimental run the pressure is first stepwise increased from ambient pressure to 6 bar(a) for each gas or gas mixture, and then stepwise decreased again to ambient pressure, according to the procedure reported previously [42]. After each step, a new steady state is quickly reached in less than 10 min (Figure SI11), and the permeability is calculated from the new plateau value. The stage cut is kept close to or below 1% to assure that polarization phenomena are negligible.

3.2.1.1. Pressure dependence of mixed gas permeation. Over the pressure interval of 1–6 bar(a), the mixed gas selectivity for CO_2/CH_4 and CO_2/N_2 (Fig. 6) is slightly higher than the ideal selectivity (Figure SI12). Upon a gradual increase of the pressure, the trend is typical for that of materials with dual-mode sorption behaviour: the CO_2 permeability decreases with pressure as a result of the saturation of the Langmuir sorption sites. Methane is not much affected, and therefore the selectivity also decreases, while N_2 decreases much less, leaving the selectivity nearly constant. In a single stage, the CO_2 concentration increases from 35% and 15% in the feed to approximately 88% and 74% in the permeate, for the CO_2/CH_4 and CO_2/N_2 mixtures, respectively. The presence of 80–90% relative humidity in the feed
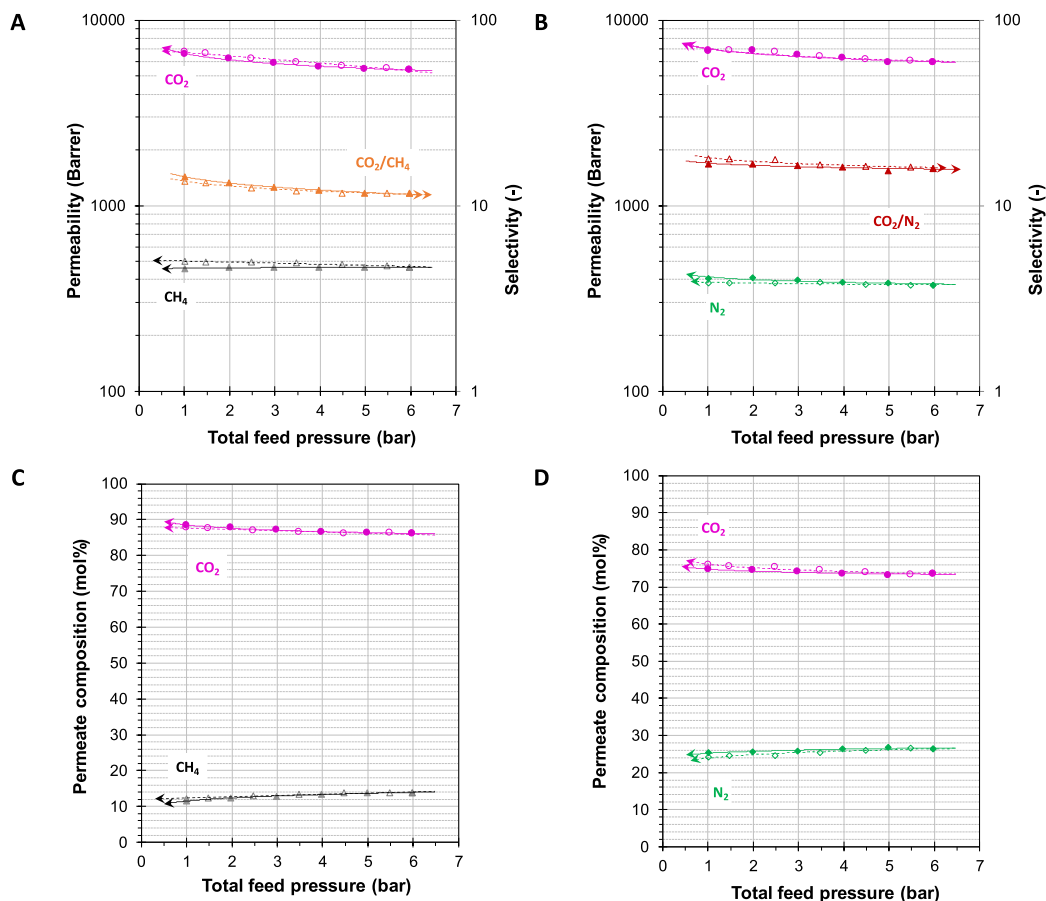

Fig. 6. Mixed gas permeation of humid gas mixtures in the stabilised membrane as a function of the total feed pressure at a relative humidity in the range of 80–90%. (A) Mixture CO_2/CH_4 (35/65 vol%) simulating biogas, and (B) Mixture CO_2/N_2 (15/85 vol%) simulating a typical flue gas composition. (C) and (D) Maximum achievable permeate compositions under optimum conditions of low stage cut and low partial pressure in the permeate (excluding the sweeping gas). Closed symbols represent the stepwise increasing pressure; open symbols represent the subsequent stepwise decreasing pressure. Lines are plotted as a guide to the eye.
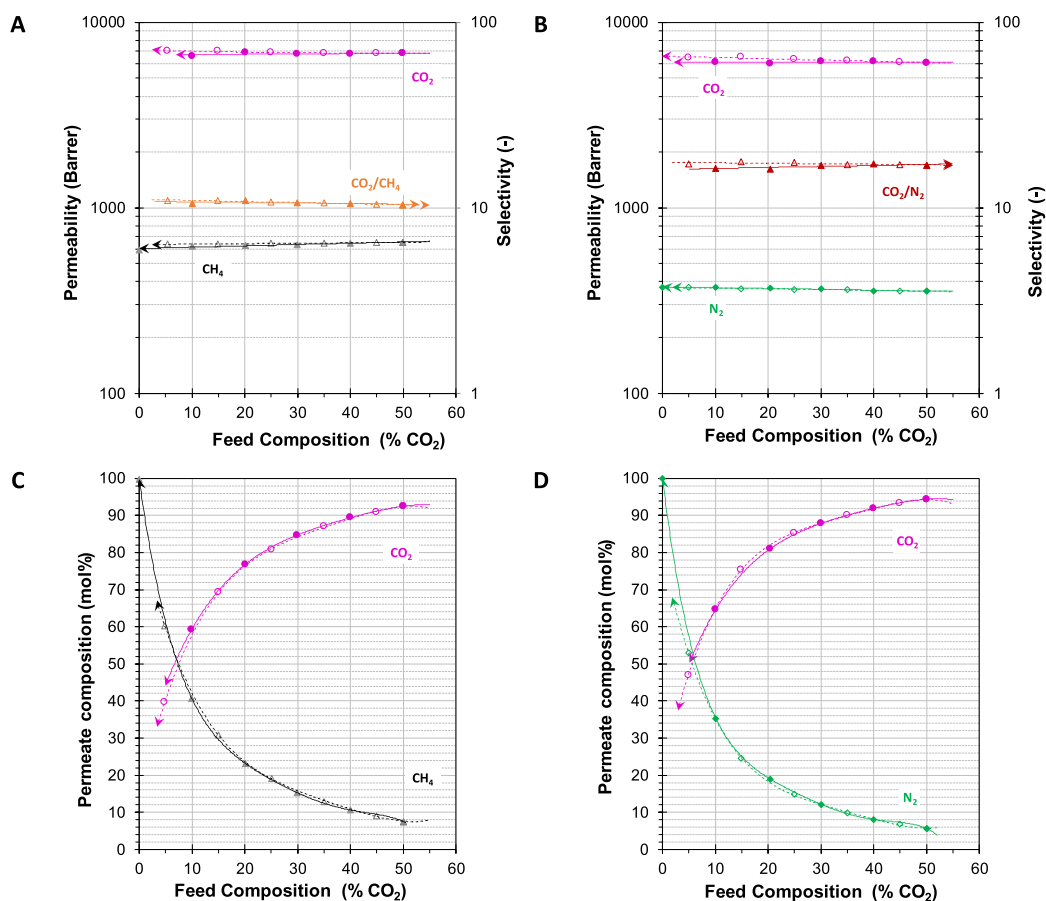
Fig. 7. Mixed gas permeation tests at 3 bar(a) feed pressure on the stabilised membrane, using humid gases at a relative humidity in the range of 80–90% and variable feed composition. (A) Mixture CO_2/CH_4 (0–50% CO_2) (B) Mixture CO_2/N_2 (0–50% CO_2) (C) and (D) Maximum achievable permeate compositions under optimum conditions of low stage cut and low partial pressure in the permeate (excluding the sweeping gas). Curves are plotted as a guide to the eye. Closed symbols represent the stepwise increasing CO_2 partial pressure; open symbols represent the subsequent stepwise decreasing CO_2 partial pressure.

gas reduces the CO_2 permeance only slightly, and hardly affects the selectivity. In comparison, PIM-1 performance is much more affected by the presence of humidity in the feed stream [36,81], and this is attributed to the competitive transport of water vapour and permanent gases [82]. This small effect of humidity on the PIM-2 membrane is due to the fluorinated structure of the polymer, its hydrophobicity and low water sorption (Fig. 4D). This behaviour is in line with that of the high the free volume glassy perfluoropolymers Hyflon AD and Teflon AF, where the decrease in CO_2 and CH_4 permeability was very low in the presence of 80% relative humidity (10–12% in Teflon AF 1600 and less than 5% in Hyflon AD 60X) [83].

The results of PIM-2 offer interesting perspectives for its use as a highly permeable membrane material that does not need any pre-treatment to de-humidify the feed gas stream. Whereas CO_2, N_2 and CH_4 permeation are hardly affected by the presence of water, the permeation of water itself gives a weak but significant signal (Figure SI13). Its kinetics are similar to those observed earlier in the sorption experiments (Fig. 4) and during the time lag measurements in the fixed volume setup (Figure SI6). Figure SI13 shows that after 1 hour of permeation, the water signal is already strongly levelling off and after a small and almost immediate initial step, the CO_2 signal is constant in this interval. This suggests that significant changes in the membrane performance upon long-term exposure to humidity should not be expected.

3.2.1.2. Composition dependence of mixed gas permeation. Under the given conditions, the change in the composition of the feed gas mixture hardly affects the individual permeabilities of the stabilised film under humid (Fig. 7A and B)

and dry conditions (Figure SI13 and Figure SI14). As a result, the permeate composition reflects that of the feed, and the CO_2 concentration in the permeate strongly increases with increasing CO_2 partial pressure in the feed. Thus, under the ideal conditions with high feed flow rate (low stage-cut) and a relatively high sweep flow rate (low partial pressure of the gases in the permeate), the CO_2 concentration increases from 10% in the feed to approximately 60% in the permeate, or from 50% in the feed to almost 95% in the permeate (Fig. 7C and D). The membrane performance is also maintained at lower feed flow, in both dry and wet conditions (Figure SI15), which confirms that polarization phenomena should be negligible.

Interestingly, the mixed gas permeabilities are systematically higher than the pure gas permeabilities measured in the time lag setup and are close to the values of the freshly methanol treated sample, which is best visible in the Robeson diagrams shown in Fig. 8. For pure gases, the sample loses some of the CO_2 permeability upon stabilization/ageing, and this is compensated by an increase in selectivity, maintaining a position very close to the Robeson 2008 upper bound. Under the conditions for mixed gases, the stabilised sample lies close to the 2018 upper bound reported for CO_2/CH_4 mixture conditions at a CO_2 partial pressure of 10 bar [21].

3.2.1.3. Time dependence of the membrane performance. Since most of the permeability measurements were performed on the same samples at different times, the effect of their history cannot be ignored. In our case, the measurements were performed in the order 1) dry mixtures, 2) pure gases, 3) humid mixtures, 4) dry mixtures again (Figure SI18). Between tests 1 and 2, additional experiments were performed as a function of the feed composition at 3 and 6 bar(a) (Figure SI15), and between tests 3 and
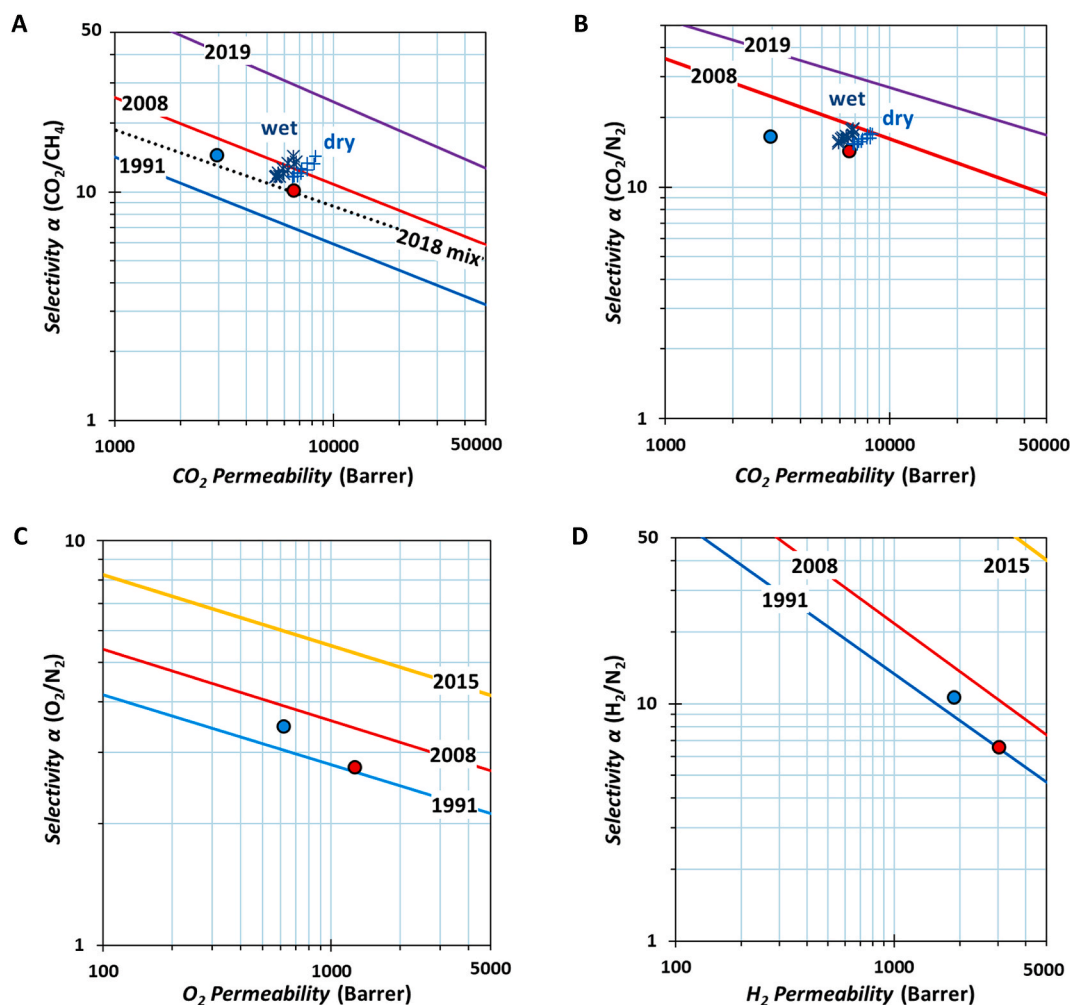
Fig. 8. Robeson plots for CO_2/CH_4 (A), CO_2/N_2 (B), O_2/N_2 (C) and H_2/N_2 (D) with the 1991 [5] upper bounds indicated by a blue line, 2008 [8] by a red line, 2015 [9] by a yellow line, 2019 [10] by purple lines, and that proposed in 2018 [21] for the CO_2/CH_4 mixture (10 bar CO_2 partial pressure at 35 °C) by a black dotted line. Filled red circles show the data for freshly methanol treated PIM-2, filled blue circles show the data for the PIM-2 membrane dried at 30 °C for 72 h under vacuum after methanol treatment measured on the fixed volume time lag setup. The + symbols represent the mixed gas permeation data with dry feed gas, plotted in Figure SI14, and the **x** symbols represent the mixed gas permeation data with humidified feed gas, plotted in Fig. 6, for the CO_2/CH_4 (35/65 vol%) and CO_2/N_2 (15/85 vol%) gas mixtures. (For interpretation of the references to colour in this figure legend, the reader is referred to the Web version of this article.)

4 additional measurements were performed as a function of the feed composition at 3 bar(a) (Figure SI16). The interpretation of the effect of the measurement conditions is therefore somewhat complicated because of unavoidable simultaneous ageing phenomena. Physical ageing is well-known in PIMs [84], and the related decrease of the excess free volume leads to a reduction of permeability as a function of time, often accompanied with an increase in selectivity, and with little effect on the gas solubility [85]. The first mixed gas permeability measurements were performed on a stabilised sample (step 1), and from the strong hysteresis in the subsequent pure CO_2 curve (step 2), it appears that swelling takes place at higher CO_2 pressures and it is likely that this partially counteracts the effect of the previous sample conditioning and ageing. The largest drop in CO_2 permeability then occurs when measuring the humid gas permeability for both mixtures (step 3), but this corresponds also to the longest time interval. Water vapour is not responsible for this lower permeability with the humid gas, as can be seen from the in-line measurement of the effect of humidity (Figure SI13B), where water vapour causes only a minor instantaneous change in the CO_2 and CH_4 permeability of less than 10%. The difference in the CO_2 permeability between step 2 and step 3 is, therefore, most likely caused by simple physical ageing of the sample, regardless the measurement conditions. Indeed, Tiwari et al. found that the presence of water vapour does not

necessarily have a negative effect, as it might even slow down physical ageing in PIM-1 [86].

4. Conclusions

In this work, the partially fluorinated polymer of intrinsic microporosity, PIM-2, confirmed to be a promising candidate as a membrane material for the separation of important gas mixtures such as flue gas (CO_2/N_2 separation) and biogas or natural gas (CO_2/CH_4 separation). Computational gas sorption results are in good agreement with experimental data. The molecular model confirms a very high fractional free volume (34%) with interconnected void structure, and high BET surface area ($>600 \, m^2 \, g^{-1}$), which forms the basis for the high gas permeability and solubility. The gas solubility in PIM-2 is relatively low when compared to PIMs with similar high fractional free volume since the fluorine atoms prefer to establish intra and interchain halogen bonds, rather than to interact with the penetrant gas. AFM force spectroscopy measurements reveal a very high rigidity of the polymer after methanol treatment (Young's modulus >2 GPa), which further increases upon ageing. The high elastic modulus, is a result of the rigid ladder-like polymer backbone in combination with the halogen bonds, and is responsible for an Arrhenius type of temperature-dependence

with a strong increase in the activation energy for diffusion with increasing gas molecular size, and thus for the strong size-selective properties of the polymer.

Readily condensable gases such as CO_2, and to a lesser extent CH_4, show distinct dual-mode sorption behaviour, typical for rigid materials with permanent microporosity, such as PIMs. As a result, in mixed gas permeation experiments, the permeability and selectivity tend to decrease with increasing feed pressure. The highly polar water vapour has a relatively low solubility in the fluorinated polymer matrix compared to the permanent gases. Therefore, the performance of the membranes is hardly affected by the presence of humidity in the feed stream, and this offers interesting perspectives for the treatment of humid gas streams such as biogas or flue gas, without the need for prior dehydration.

Acknowledgements

Appendix A. Supplementary data

Supplementary data to this article can be found online at https:// doi.org/10.1016/j.memsci.2019.117460.

References

[1] T.C. Merkel, H. Lin, X. Wei, R. Baker, Power plant post-combustion carbon dioxide capture: an opportunity for membranes, J. Membr. Sci. 359 (2010) 126–139, https://doi.org/10.1016/j.memsci.2009.10.041.

[2] P. Maas, N. Nauels, L. Zhao, P. Markewitz, V. Scherer, M. Modigell, D. Stolten, J.-F. Hake, Energetic and economic evaluation of membrane-based carbon capture routes for power plant processes, Int. J. Greenh. Gas Control 44 (2016) 124–139, https://doi.org/10.1016/J.IJGGC.2015.11.018.

[3] S.E. Kentish, 110th anniversary: process developments in carbon dioxide capture using membrane technology, Ind. Eng. Chem. Res. 0 (2019), https://doi.org/10. 1021/acs.iecr.9b02013 null-null.

[4] M.-C. Ferrari, D. Bocciardo, S. Brandani, Integration of multi-stage membrane carbon capture processes to coal-fired power plants using highly permeable polymers, Green Energy Environ. 1 (2016) 211–221, https://doi.org/10.1016/J.GEE.2016.10.001.

[5] L.M. Robeson, Correlation of separation factor versus permeability for polymeric membranes, J. Membr. Sci. 62 (1991) 165–185, https://doi.org/10.1016/0376-7388(91)80060-J.

[6] P.M. Budd, B.S. Ghanem, S. Makhseed, N.B. McKeown, K.J. Msayib, C.E. Tattershall, Polymers of intrinsic microporosity (PIMs): robust, solution-processable, organic nanoporous materials, Chem. Commun. 10 (2004) 230, https:// doi.org/10.1039/b311764b.

[7] P.M. Budd, E.S. Elabas, B.S. Ghanem, S. Makhseed, N.B. McKeown, K.J. Msayib, C.E. Tattershall, D. Wang, Solution-processed, organophilic membrane derived from a polymer of intrinsic microporosity, Adv. Mater. 16 (2004) 456–459, https://doi. org/10.1002/adma.200306053.

[8] L.M. Robeson, The upper bound revisited, J. Membr. Sci. 320 (2008) 390–400, https://doi.org/10.1016/j.memsci.2008.04.030.

[9] R. Swaidan, B. Ghanem, I. Pinnau, Fine-tuned intrinsically ultramicroporous polymers redefine the permeability/selectivity upper bounds of membrane-based air and hydrogen separations, ACS Macro Lett. 4 (2015) 947–951, https://doi.org/10. 1021/acsmacrolett.5b00512.

[10] B. Comesaña-Gándara, J. Chen, C.G. Bezzu, M. Carta, I. Rose, M.-C. Ferrari, E. Esposito, A. Fuoco, J.C. Jansen, N.B. McKeown, Redefining the Robeson upper bounds for CO 2/CH 4 and CO 2/N 2 separations using a series of ultrapermeable benzotriptycene-based polymers of intrinsic microporosity, Energy Environ. Sci. 12 (2019) 2733–2740, https://doi.org/10.1039/C9EE01384A.

[11] R.W. Baker, K. Lokhandwala, Natural gas processing with membranes: an overview, Ind. Eng. Chem. Res. 47 (2008) 2109–2121, https://doi.org/10.1021/ie071083w.

[12] M. Kárászová, Z. Sedláková, P. Izák, Review: gas permeation processes in biogas upgrading: a short review, Chem. Pap. (2015), https://doi.org/10.1515/chempap-2015-0141.

[13] X.Y. Chen, H. Vinh-Thang, A.A. Ramirez, D. Rodrigue, S. Kaliaguine, Membrane gas separation technologies for biogas upgrading, RSC Adv. (2015), https://doi.org/10. 1039/c5ra00666j.

[14] E. Esposito, L. Dellamuzia, U. Moretti, A. Fuoco, L. Giorno, J.C. Jansen, Simultaneous production of biomethane and food grade CO 2 from biogas: an industrial case study, Energy Environ. Sci. 12 (2019) 281–289, https://doi.org/10. 1039/C8EE02897D.

[15] L. Zhao, E. Riensche, R. Menzer, L. Blum, D. Stolten, A parametric study of CO2/N2 gas separation membrane processes for post-combustion capture, J. Membr. Sci. 325 (2008) 284–294, https://doi.org/10.1016/J.MEMSCI.2008.07.058.

[16] D.M. D'Alessandro, B. Smit, J.R. Long, Carbon dioxide capture: prospects for new materials, Angew. Chem. Int. Ed. (2010), https://doi.org/10.1002/anie.201000431.

[17] U.W.R. Siagian, A. Raksajati, N.F. Himma, K. Khoiruddin, I.G. Wenten, Membrane-based carbon capture technologies: membrane gas separation vs. Membrane contactor, J. Nat. Gas Sci. Eng. (2019), https://doi.org/10.1016/j.jngse.2019.04.008.

[18] M. Kárászová, J. Vejražka, V. Veselý, K. Friess, A. Randová, V. Hejtmánek, L. Brabec, P. Izák, A water-swollen thin film composite membrane for effective upgrading of raw biogas by methane, Separ. Purif. Technol. 89 (2012) 212–216, https://doi.org/10.1016/j.seppur.2012.01.037.

[19] P. Dolejš, V. Poštulka, Z. Sedláková, V. Jandová, J. Vejražka, E. Esposito, J.C. Jansen, P. Izák, Simultaneous hydrogen sulphide and carbon dioxide removal from biogas by water–swollen reverse osmosis membrane, Separ. Purif. Technol. 131 (2014) 108–116, https://doi.org/10.1016/j.seppur.2014.04.041.

[20] Z. Sedláková, M. Kárászová, J. Vejražka, L. Morávková, E. Esposito, A. Fuoco, J.C. Jansen, P. Izák, Biomethane production from biogas by separation using thin-film composite membranes, Chem. Eng. Technol. 40 (2017) 821–828, https://doi. org/10.1002/ceat.201600612.

[21] Y. Wang, X. Ma, B.S. Ghanem, F. Alghunaimi, I. Pinnau, Y. Han, Polymers of intrinsic microporosity for energy-intensive membrane-based gas separations, Mater. Today Nano. 3 (2018) 69–95, https://doi.org/10.1016/J.MTNANO.2018.11.003.

[22] Y. Rogan, L. Starannikova, V. Ryzhikh, Y. Yampolskii, P. Bernardo, F. Bazzarelli, J.C. Jansen, N.B. McKeown, Synthesis and gas permeation properties of novel spirobisindane-based polyimides of intrinsic microporosity, Polym. Chem. 4 (2013) 3813, https://doi.org/10.1039/c3py00451a.

[23] M. Carta, R. Malpass-Evans, M. Croad, Y. Rogan, J.C. Jansen, P. Bernardo, F. Bazzarelli, N.B. McKeown, An efficient polymer molecular sieve for membrane gas separations, Science 339 (80) (2013) 303–307, https://doi.org/10.1126/ science.1228032.

[24] R. Williams, L.A. Burt, E. Esposito, J.C. Jansen, E. Tocci, C. Rizzuto, M. Lanč, M. Carta, N.B. McKeown, A highly rigid and gas selective methanopentacene-based polymer of intrinsic microporosity derived from Tröger's base polymerization, J. Mater. A. 6 (2018) 5661–5667, https://doi.org/10.1039/C8TA00509E.

[25] M. Carta, P. Bernardo, G. Clarizia, J.C. Jansen, N.B. McKeown, Gas permeability of hexaphenylbenzene based polymers of intrinsic microporosity, Macromolecules 47 (2014) 8320–8327, https://doi.org/10.1021/ma501925j.

[26] I. Rose, C.G. Bezzu, M. Carta, B. Comesaña-Gándara, E. Lasseuguette, M.C. Ferrari, P. Bernardo, G. Clarizia, A. Fuoco, J.C. Jansen, K.E. Hart, T.P. Liyana-Arachchi, C.M. Colina, N.B. McKeown, Polymer ultrapermeability from the inefficient packing of 2D chains, Nat. Mater. 16 (2017) 932–937, https://doi.org/10.1038/nmat4939.

[27] R. Swaidan, B.S. Ghanem, E. Litwiller, I. Pinnau, Pure- and mixed-gas CO2/CH4 separation properties of PIM-1 and an amidoxime-functionalized PIM-1, J. Membr. Sci. 457 (2014) 95–102, https://doi.org/10.1016/j.memsci.2014.01.055.

[28] C.R. Mason, L. Maynard-Atem, N.M. Al-Harbi, P.M. Budd, P. Bernardo, F. Bazzarelli, G. Clarizia, J.C. Jansen, Polymer of intrinsic microporosity incorporating thioamide functionality: preparation and gas transport properties, Macromolecules 44 (2011) 6471–6479, https://doi.org/10.1021/ma200918h.

[29] N. Du, G.P. Robertson, J. Song, I. Pinnau, M.D. Guiver, High-performance carboxylated polymers of intrinsic microporosity (PIMs) with tunable gas transport properties, Macromolecules 42 (2009) 6038–6043, https://doi.org/10.1021/ma9009017.

[30] M. Macchione, J.C. Jansen, G. De Luca, E. Tocci, M. Longeri, E. Drioli, Experimental analysis and simulation of the gas transport in dense Hyflon® AD60X membranes: influence of residual solvent, Polymer (Guildf) 48 (2007) 2619–2635, https://doi. org/10.1016/j.polymer.2007.02.068.

[31] G. Kupgan, L.J. Abbott, K.E. Hart, C.M. Colina, Modeling amorphous microporous polymers for CO2 capture and separations, Chem. Rev. (2018) 5488–5538, https:// doi.org/10.1021/acs.chemrev.7b00691.

[32] B. Satilmis, M. Lanč, A. Fuoco, C. Rizzuto, E. Tocci, P. Bernardo, G. Clarizia, E. Esposito, M. Monteleone, M. Dendisová, K. Friess, P.M. Budd, J.C. Jansen, Temperature and pressure dependence of gas permeation in amine-modified PIM-1, J. Membr. Sci. 555 (2018) 483–496, https://doi.org/10.1016/j.memsci.2018.03.039.

[33] R.M. Venable, A. Krämer, R.W. Pastor, Molecular dynamics simulations of membrane permeability, Chem. Rev. (2019), https://doi.org/10.1021/acs.chemrev.8b00486.

[34] H. Sato, S. Nakajo, Y. Oishi, Y. Shibasaki, Synthesis of linear polymer of intrinsic microporosity from 5,5′,6,6′-tetrahydroxy-3,3,3′,3′-tetramethylspirobisindane and decafluorobiphenyl, React. Funct. Polym. 125 (2018) 70–76, https://doi.org/10. 1016/J.REACTFUNCTPOLYM.2018.02.006.

[35] B. Satilmis, T. Uyar, Development of superhydrophobic electrospun fibrous membrane of polymers of intrinsic microporosity (PIM-2), Eur. Polym. J. 112 (2019) 87–94, https://doi.org/10.1016/J.EURPOLYMJ.2018.12.029.

[36] E. Lasseuguette, M. Carta, S. Brandani, M.-C. Ferrari, Effect of humidity and flue gas impurities on CO2 permeation of a polymer of intrinsic microporosity for post-combustion capture, Int. J. Greenh. Gas Control 50 (2016) 93–99, https://doi.org/ 10.1016/J.IJGGC.2016.04.023.

[37] P.M. Budd, N.B. McKeown, B.S. Ghanem, K.J. Msayib, D. Fritsch, L. Starannikova, N. Belov, O. Sanfirova, Y. Yampolskii, V. Shantarovich, Gas permeation parameters and other physicochemical properties of a polymer of intrinsic microporosity: polybenzodioxane PIM-1, J. Membr. Sci. 325 (2008) 851–860, https://doi.org/10. 1016/j.memsci.2008.09.010.

[38] M. Longo, M.P. De Santo, E. Esposito, A. Fuoco, M. Monteleone, L. Giorno, J.C. Jansen, Force spectroscopy determination of Young's modulus in mixed matrix membranes, Polymer (Guildf). 156 (2018) 22–29, https://doi.org/10.1016/j.

polymer.2018.09.043.

[39] Bruker AFM Probes: Force Calibration Cantilevers, Support Note 013-000-000, in: n.d.: pp. 1–6.

[40] H. Hertz, Ueber die Berührung fester elastischer Körper, J. für die Reine Angewandte Math. 92 (1882) 156–171.

[41] G.N. Greaves, A.L. Greer, R.S. Lakes, T. Rouxel, Poisson's ratio and modern materials, Nat. Mater. 10 (2011) 823–837, https://doi.org/10.1038/nmat3134.

[42] S.C. Fraga, M. Monteleone, M. Lanč, E. Esposito, A. Fuoco, L. Giorno, K. Pilnáček, K. Friess, M. Carta, N.B. McKeown, P. Izák, Z. Petrusová, J.G. Crespo, C. Brazinha, J.C. Jansen, A novel time lag method for the analysis of mixed gas diffusion in polymeric membranes by on-line mass spectrometry: method development and validation, J. Membr. Sci. 561 (2018) 39–58, https://doi.org/10.1016/j.memsci.2018.04.029.

[43] M. Monteleone, E. Esposito, A. Fuoco, M. Lanč, K. Pilnáček, K. Friess, C. Bezzu, M. Carta, N. McKeown, J.C. Jansen, A novel time lag method for the analysis of mixed gas diffusion in polymeric membranes by on-line mass spectrometry: pressure dependence of transport parameters, Membranes (Basel) 8 (2018) 73, https://doi.org/10.3390/membranes8030073.

[44] K. Friess, V. Hynek, M. Šípek, W.M. Kujawski, O. Vopička, M. Zgažar, M.W. Kujawski, Permeation and sorption properties of poly(ether-block-amide) membranes filled by two types of zeolites, Separ. Purif. Technol. 80 (2011) 418–427, https://doi.org/10.1016/j.seppur.2011.04.012.

[45] P. U. G. P. s Accelrys Software Inc, BIOVIA (Ex Material Studio 7.0) Package. Classical Simulation Theory Section, Sorption User Guide., 2013.

[46] H. Sun, COMPASS: an ab initio force-field optimized for condensed-phase ApplicationsOverview with details on alkane and benzene compounds, J. Phys. Chem. B 102 (1998) 7338–7364.

[47] C. Rizzuto, A. Caravella, A. Brunetti, C.H. Park, Y.M. Lee, E. Drioli, G. Barbieri, E. Tocci, Sorption and Diffusion of CO_2/N_2 in gas mixture in thermally-rearranged polymeric membranes: a molecular investigation, J. Membr. Sci. 528 (2017) 135–146, https://doi.org/10.1016/J.MEMSCI.2017.01.025.

[48] C.H. Park, E. Tocci, S. Kim, A. Kumar, Y.M. Lee, E. Drioli, A simulation study on OH-containing polyimide (HPI) and thermally rearranged polybenzoxazoles (TR-PBO): relationship between gas transport properties and free volume morphology, J. Phys. Chem. B 118 (2014) 2746–2757, https://doi.org/10.1021/jp411612g.

[49] L. Zhao, D. Zhai, B. Liu, Z. Liu, C. Xu, W. Wei, Y. Chen, J. Gao, Grand Canonical Monte Carlo simulations for energy gases on PIM-1 polymer and silicalite-1, Chem. Eng. Sci. 68 (2012) 101–107 https://doi.org/10.1016/j.ces.2011.09.017.

[50] O. Hölck, M. Böhning, M. Heuchel, M.R. Siegert, D. Hofmann, Gas sorption isotherms in swelling glassy polymers—Detailed atomistic simulations, J. Membr. Sci. 428 (2013) 523–532 https://doi.org/10.1016/j.memsci.2012.10.023.

[51] P.J. Flory, M. Volkenstein, Statistical mechanics of chain molecules, Biopolymers 8 (1969) 699–700, https://doi.org/10.1002/bip.1969.360080514.

[52] D. Hofmann, L. Fritz, J. Ulbrich, D. Paul, Molecular simulation of small molecule diffusion and solution in dense amorphous polysiloxanes and polyimides, Comput. Theor. Polym. Sci. 10 (2000) 419–436.

[53] E. Tocci, P. Pullumbi, Molecular simulation of realistic membrane models of alkylated PEEK membranes, Mol. Simul. 32 (2006) 145–154, https://doi.org/10.1080/08927020600654645.

[54] J.Y. Park, D.R. Paul, Correlation and prediction of gas permeability in glassy polymer membrane materials via a modified free volume based group contribution method, J. Membr. Sci. 125 (1997) 23–39, https://doi.org/10.1016/S0376-7388(96)00061-0.

[55] A. Bondi, van der Waals volumes and radii, J. Phys. Chem. 68 (1964) 441–451, https://doi.org/10.1021/j100785a001.

[56] V. Teplyakov, P. Meares, Correlation aspects of the selective gas permeabilities of polymeric materials and membranes, Gas Sep. Purif. 4 (1990) 66–74, https://doi.org/10.1016/0950-4214(90)80030-O.

[57] J.I. Siepmann, D. Frenkel, Configurational bias Monte Carlo: a new sampling scheme for flexible chains, Mol. Phys. 75 (1992) 59–70, https://doi.org/10.1080/00268979200100061.

[58] Florian Müller-Plathe, Molecular dynamics simulation of gas transport in amorphous polypropylene, J. Chem. Phys. 96 (1992) 3200–3205 https://doi.org/10.1063/1.461963.

[59] C.S. Chassapis, J.K. Petrou, J.H. Petropoulos, D.N. Theodorou, Analysis of computed trajectories of penetrant micromolecules in a simulated polymeric material, Macromolecules 29 (1996) 3615–3624, https://doi.org/10.1021/ma951474z.

[60] T.a. Andrea, W.C. Swope, H.C. Andersen, The role of long ranged forces in determining the structure and properties of liquid water, J. Chem. Phys. 79 (1983) 4576–4584, https://doi.org/10.1063/1.446373.

[61] H.J.C. Berendsen, J.P.M. Postma, W.F. van Gunsteren, a DiNola, J.R. Haak, Molecular dynamics with coupling to an external bath, J. Chem. Phys. 81 (1984) 3684–3690, https://doi.org/10.1063/1.448118.

[62] J.M. Haile, Molecular Dynamics Simulation: Elementary Methods, Wiley, New York, 1997.

[63] J. Zhang, J. Jin, R. Cooney, Q. Fu, G.G. Qiao, S. Thomas, T.C. Merkel, Synthesis of perfectly alternating copolymers for polymers of intrinsic microporosity, Polym. Chem. 6 (2015) 5003–5008, https://doi.org/10.1039/C5PY00570A.

[64] I. Rose, M. Carta, R. Malpass-Evans, M.-C. Ferrari, P. Bernardo, G. Clarizia, J.C. Jansen, N.B. McKeown, Highly permeable benzotriptycene-based polymer of intrinsic microporosity, ACS Macro Lett. 4 (2015) 912–915, https://doi.org/10.1021/acsmacrolett.5b00439.

[65] W. Fang, L. Zhang, J. Jiang, Polymers of intrinsic microporosity for gas permeation:

[66] E. Tocci, L. De Lorenzo, P. Bernardo, G. Clarizia, F. Bazzarelli, N.B. Mckeown, M. Carta, R. Malpass-Evans, K. Friess, K. Pilnáček, M. Lanč, Y.P. Yampolskii, L. Strarannikova, V. Shantarovich, M. Mauri, J.C. Jansen, Molecular modeling and gas permeation properties of a polymer of intrinsic microporosity composed of ethanoanthracene and tröger's base units, Macromolecules 47 (2014) 7900–7916, https://doi.org/10.1021/ma501469m.

[67] D.W. Breck, Zeolite Molecular Sieves: Structure, Chemistry, and Use, John Wiley & Sons, New York, N. Y., 1974, https://doi.org/10.1093/chromsci/13.4.18A-c.

[68] A. Fuoco, C. Rizzuto, E. Tocci, M. Monteleone, E. Esposito, P.M. Budd, M. Carta, B. Comesaña-Gándara, N.B. McKeown, J.C. Jansen, The origin of size-selective gas transport through Polymers of Intrinsic Microporosity, online, J. Mater. Chem. A 7 (2019) 20121–20126, https://doi.org/10.1039/c9ta07159h.

[69] C.G. Bezzu, M. Carta, M.-C. Ferrari, J.C. Jansen, M. Monteleone, E. Esposito, A. Fuoco, K. Hart, T.P. Liyana-Arachchi, C.M. Colina, N.B. McKeown, The synthesis, chain-packing simulation and long-term gas permeability of highly selective spirobifluorene-based polymers of intrinsic microporosity, J. Mater. Chem. A. 6 (2018) 10507–10514, https://doi.org/10.1039/C8TA02601G.

[70] M.R. Khdhayyer, E. Esposito, A. Fuoco, M. Monteleone, L. Giorno, J.C. Jansen, M.P. Attfield, P.M. Budd, Mixed matrix membranes based on UiO-66 MOFs in the polymer of intrinsic microporosity PIM-1, Separ. Purif. Technol. 173 (2017) 304–313, https://doi.org/10.1016/j.seppur.2016.09.036.

[71] A. Fuoco, M. Khdhayyer, M. Attfield, E. Esposito, J.C. Jansen, P. Budd, Synthesis and transport properties of novel MOF/PIM-1/MOF sandwich membranes for gas separation, Membranes (Basel) 7 (2017) 7, https://doi.org/10.3390/membranes7010007.

[72] M. Khdhayyer, A.F. Bushell, P.M. Budd, M.P. Attfield, D. Jiang, A.D. Burrows, E. Esposito, P. Bernardo, M. Monteleone, A. Fuoco, G. Clarizia, F. Bazzarelli, A. Gordano, J.C. Jansen, Mixed matrix membranes based on MIL-101 metal–organic frameworks in polymer of intrinsic microporosity PIM-1, Separ. Purif. Technol. 212 (2019) 545–554, https://doi.org/10.1016/j.seppur.2018.11.055.

[73] J.C. Jansen, K. Friess, E. Drioli, Organic vapour transport in glassy perfluoropolymer membranes: a simple semi-quantitative approach to analyze clustering phenomena by time lag measurements, J. Membr. Sci. 367 (2011) 141–151, https://doi.org/10.1016/j.memsci.2010.10.063.

[74] K. Friess, J.C. Jansen, J. Požívil, V. Hanta, V. Hynek, O. Vopička, M. Zgažar, P. Bernardo, P. Izák, E. Drioli, Anomalous permeation and sorption of C 1 –C 6 alcohol vapors in Teflon AF 2400, Ind. Eng. Chem. Res. 52 (2013) 10406–10417, https://doi.org/10.1021/ie303013y.

[75] Y. Yampolskii, I. Pinnau, B.D. Freeman, Materials Science of Membranes for Gas and Vapor Separation, John Wiley & Sons, Ltd, Chichester, UK, 2006, https://doi.org/10.1002/047002903X.

[76] D. Nikolaeva, I. Azcune, M. Tanczyk, K. Warmuzinski, M. Jaschik, M. Sandru, P.I. Dahl, A. Genua, S. Loïs, E. Sheridan, A. Fuoco, I.F.J. Vankelecom, The performance of affordable and stable cellulose-based poly-ionic membranes in CO_2/N_2 and CO_2/CH_4 gas separation, J. Membr. Sci. 564 (2018) 552–561, https://doi.org/10.1016/j.memsci.2018.07.057.

[77] A. Petersson, A. Wellinger, Biogas upgrading technologies–developments and innovations, IEA Bioenergy (2009) 20, https://doi.org/10.1016/j.wasman.2011.09.003.

[78] A. Fuoco, B. Comesaña-Gándara, M. Longo, E. Esposito, M. Monteleone, I. Rose, C.G. Bezzu, M. Carta, N.B. McKeown, J.C. Jansen, Temperature dependence of gas permeation and diffusion in triptycene-based ultrapermeable polymers of intrinsic microporosity, ACS Appl. Mater. Interfaces 10 (2018) 36475–36482, https://doi.org/10.1021/acsami.8b13634.

[80] W.J. Koros, C. Zhang, Materials for next-generation molecularly selective synthetic membranes, Nat. Mater. (2017), https://doi.org/10.1038/nmat4805.

[81] E. Lasseuguette, M.-C. Ferrari, S. Brandani, Humidity impact on the gas permeability of PIM-1 membrane for post-combustion application, Energy Procedia 63 (2014) 194–201, https://doi.org/10.1016/J.EGYPRO.2014.11.020.

[82] C.A. Scholes, J. Jin, G.W. Stevens, S.E. Kentish, Competitive permeation of gas and water vapour in high free volume polymeric membranes, J. Polym. Sci., Part B: Polym. Phys. 53 (2015) 719–728, https://doi.org/10.1002/polb.23689.

[83] C.A. Scholes, S. Kanehashi, G.W. Stevens, S.E. Kentish, Water permeability and competitive permeation with CO_2 and CH_4 in perfluorinated polymeric membranes, Separ. Purif. Technol. 147 (2015) 203–209, https://doi.org/10.1016/j.seppur.2015.04.023.

[84] Z.-X. Low, P.M. Budd, N.B. McKeown, D.A. Patterson, Gas permeation properties, physical aging, and its mitigation in high free volume glassy polymers, Chem. Rev. 118 (2018) 5871–5911, https://doi.org/10.1021/acs.chemrev.7b00629.

[85] P. Bernardo, F. Bazzarelli, F. Tasselli, G. Clarizia, C.R. Mason, L. Maynard-Atem, P.M. Budd, M. Lanč, K. Pilnáček, O. Vopička, K. Friess, D. Fritsch, Y.P. Yampolskii, V. Shantarovich, J.C. Jansen, Effect of physical aging on the gas transport and sorption in PIM-1 membranes, Polymer (Guildf). 113 (2017) 283–294, https://doi.org/10.1016/j.polymer.2016.10.040.

[86] R.R. Tiwari, J. Jin, B.D. Freeman, D.R. Paul, Physical aging, CO_2 sorption and plasticization in thin films of polymer with intrinsic microporosity (PIM-1), J. Membr. Sci. 537 (2017) 362–371, https://doi.org/10.1016/j.memsci.2017.04.069.

[87] P. Li, T.S. Chung, D.R. Paul, Temperature dependence of gas sorption and permeation in PIM-1, J. Membr. Sci. 450 (2014) 380–388, https://doi.org/10.1016/j.memsci.2013.09.030.